Springer

Acta Mechanica Sinica

CrossMark click for updates

·RESEARCH PAPER·

Acta Mech. Sin., Vol. 38, 321563 (2022)
https://doi.org/10.1007/s10409-022-09029-3

Study on prediction model of cavitation erosion incubation period of duplex stainless steel surfacing layer in a benign medium

Yefeng Bao[1*], Chong Cao[1], Bingqi Xie[1,2], Qining Song[1], Yongfeng Jiang[1], and Nan Xu[1]

[1] *College of Mechanical and Electrical Engineering, Hohai University, Changzhou 213022, China;*
[2] *Fujian Fuqing Nuclear power Co., Ltd, Fuqing 350300, China*

Received December 30, 2021; accepted January 24, 2022; published online April 2, 2022

In order to estimate the cavitation incubation period of duplex stainless steel (DSS) under ultrasonic cavitation erosion (CE), this paper analyzed the loading process of material during ultrasonic CE. Local strain theory, cumulative damage theory, and Bernoulli probability model were used to derive the minimum number of cavitation impacts required for the initiation of fatigue cracks, and the predictive equation of the material cavitation incubation period was given. DSS was obtained by tungsten inert gas welding (TIG) powder surfacing method. Tensile test and ultrasonic CE test were performed, and the tensile test data were used to calculate the cavitation incubation period by using the predictive equation. Due to the possible presence of precipitates and micro-cracks in the sample, there was an error between the calculated and the test results. The results showed that the max error between the calculated results and the test results was 8.1%, and the errors of the remaining two groups were within 3.5%.

Duplex stainless steel, Ultrasonic cavitation erosion, Incubation period, Calculation, Tensile properties

Citation: Y. Bao, C. Cao, B. Xie, Q. Song, Y. Jiang, and N. Xu, Study on prediction model of cavitation erosion incubation period of duplex stainless steel surfacing layer in a benign medium, Acta Mech. Sin. **38**, 321563 (2022), https://doi.org/10.1007/s10409-022-09029-3

Abbreviations

σ'_f	fatigue strength coefficient
$\Delta\varepsilon_e$	elastic strain
b	fatigue strength index of elastic strain zone
$\Delta\varepsilon_p$	plastic strain
ε_f	fracture ductility
C	fatigue strength index of the plastic strain zone
$\Delta\sigma$	stress amplitude
E	Young's modulus
ε	maximum strain
S	maximum stress
K	strength coefficient
n	deformation hardening index
K_t	stress concentration coefficient (it is 1 when there is no stress concentration)
S_f	fracture strength
ε_f	fracture ductility, that is elongation after fracture
D	the damage of material under a single load
N_f	fatigue life of the material under a certain load
D_t	total damage
k	number of loads of different magnitudes
N_{fi}	fatigue life of the material under the i-th load
n_i	the number of cycles that the i-th load occurs
$\Delta\sigma_j$	nominal stress of a bubble collapse
P_j	probability of occurrence of a bubble collapse with nominal stress of $\Delta\sigma_j$
N_i	the number of bubbles collapsed and impacted on a fixed position
S	damaged area left by a single bubble impacting
S_0	the total CE area of the sample
p	probability of the cavitation pit acting on a certain place
M	total number of bubbles acting on the entire cavitation zone
M_f	minimum number of impacts of bubbles required for the initiation of cavitation cracks
fc	the frequency of the impact of bubbles
t_i	the length of CE incubation period
$S_{0.2}$	true stresses corresponding to the conditional yield strength
S_m	tensile strength

*Corresponding author. E-mail address: baoyf@hhuc.edu.cn (Yefeng Bao)
Executive Editor: Chao Sun

$\varepsilon_{0.2}$ true strains corresponding to the conditional yield strength
ε_m tensile strength
σ_f fracture strength
F_f tensile force
A_f cross-sectional area of the sample after breaking
P_i probability of the occurrence of bubble collapse with a nominal stress $\Delta\sigma_i$
V_c volume of a single cavity
N_c number of cavitation bubbles generated by each vibration of ultrasonic cavitation
h distance between the ultrasonic probe and the sample
A_d area of the sample damaged by CE

1. Introduction

Cavitation erosion (CE) is a long-term damage phenomenon in flow propulsion systems, water conservancy machinery, and other flow-through components [1,2]. The turbulence and vibration caused by the collapse of the cavitation bubbles will damage the surfaces of the propellers, turbines, and hydraulic pumps, which will shorten the service life of the parts and increase the energy loss [2,3]. In recent years, many researchers conducted study on the mechanism of CE. Because of the complex characteristics of random, instantaneous, microscopic, and multiple phases of CE [4], there are many theories about the mechanism of CE. Some researchers believe that the main mechanical damage mechanisms of CE are shock waves and micro-jets, and some researchers believe that the micro-streaming [5] and shear flow [6] in the process of cavitation and collapse will also damage the surface of the material. In addition, a few researchers believe that thermal effects and corrosion in cavitation are the main reasons for CE. Currently, researchers basically determine that the failure mechanism of CE is dominated by mechanical effects [7], while thermal effects [8,9] and corrosion [10,11] also play a role. The CE process of materials can be divided into incubation period, accumulation period, stationary period, and attenuation period, and the length of the incubation period can indirectly reflect the CE resistance of material [12-14].

The microstructure of duplex stainless steels (DSSs) is composed of ferrite and austenite, and the content of ferrite or austenite is not less than 30% [15,16]. Due to the combination of the advantages of austenitic stainless steel and ferritic stainless steel, DSSs have good chloride stress corrosion resistance, good weldability, excellent toughness, and high hardness [17]. Therefore, DSSs are very suitable to be applied as a CE-resistant material. Because of excellent corrosion resistance, corrosion factors account for a small proportion of the CE process of DSSs [18]. So, it is of great significance to study the cavitation incubation period of DSS and establish the relationship between it and the mechanical properties.

Huang and Zhong [19] developed a cavitation-induced damage model to study the mechanical damage of soft materials by high-intensity focused ultrasound. Song and Cai [20] studied the cavitation dynamics in a vitrimer. Richman and McNaughton [21] studied the effect of material strain characteristics on the cavitation failure rate through cyclic deformation tests and found a good correlation between the fatigue strength coefficient and material removal rates (as shown in Eq. (1)). The amount of material removal (expressed by the mean depth of penetration) was inversely proportional to $(n'\sigma'_f)$, where n is the cyclic deformation strengthening index.

$$\sigma_a = \frac{\Delta\varepsilon_e}{2}E = \sigma'_f(2N)^b. \tag{1}$$

Among them, σ_a is the alternating load amplitude; $\frac{\Delta\varepsilon_e}{2}$ is the elastic strain amplitude; E is the modulus of elasticity; σ'_f is the fatigue strength coefficient when $2N = 1$, which is approximately equal to the tensile strength; $2N$ is the number of cycles of the fatigue test; b is the fatigue strength index.

Karimi and Leo [22] established a model to calculate CE rate. The model was a function of CE rate and mechanical properties (such as, yield strength, tensile strength, processing depth, and hardening index). Long et al. [23] combined large eddy simulation (LES) with a homogeneous cavitation model to study turbulent cavitation flow around a sphere, and the simulated accuracy has been evaluated using the LES verification and validation method. They believe that these parameters reflect the response of the material to the impact generated by the collapse of cavitation bubbles. Hattori and Ishikura [24] established a database of CE resistant materials. They used ultrasonic CE tests to study the CE resistance of different stainless steels. They found that the relationship between the CE resistance and hardness of stainless steel can be described by Eq. (2).

$$ER = 2.6 \times 10^{-7} \times (HV \times F_{\text{mat}})^{2.4}. \tag{2}$$

Among them, HV is Vickers hardness; F_{mat} is a material factor calculated from the surface hardness of the material after the cavitation test and the original surface hardness; the time required for the cavitation unit depth (h μm^{-1}) was used to define ER. As mentioned earlier, most researchers only pay attention to the relationship between cavitation damage and material properties but ignore the cavitation conditions.

This paper combined local strain theory, cumulative damage theory, and the Bernoulli probability model to derive the minimum cavitation impact number required to induce fatigue cracks in DSS. The estimating equation for the cavitation incubation period of the material was given. DSS surfacing layers were subjected to tensile and ultrasonic cavitation tests to verify the accuracy of the equation.

2. Predictive equation of CE incubation period

A single bubble acting on a particular position on the surface of the material was analyzed. When the shock wave from a bubble collapse acts on the surface of the sample, the surface within a specific thickness range is bent and deformed. The bottom of the deformed layer is subjected to tensile stress, and the top is subjected to compressive stress, as shown in Fig. 1a. Since the surrounding materials constrain the deformation area, the deformation layer can be equivalent to the bending deformation of a thin plate of a certain thickness fixed at both ends under impact load (as shown in Fig. 1b). In a fluid with a changing flow rate, the process of nucleation, growth, and collapse of cavitation bubbles is continuous and alternate. Therefore, the process of repeated action of bubbles on the surface and the formation of cracks can be approximated as the fatigue crack initiation process of the tensile deformation zone at the bottom of the smooth sample with a certain thickness.

The commonly used methods for predicting the fatigue life of metal components are mainly divided into fatigue life prediction method based on stress and fatigue life prediction method based on local strain. The stress-based fatigue life prediction method is mainly suitable for high-cycle fatigue in the elastic range [25]. However, the load on the material is distributed in a wide range during the CE process, and the material may undergo elastic deformation or plastic deformation. Therefore, the fatigue life prediction method based on stress is challenging to apply. The local strain method believes that fatigue cracks initiate from the maximum local strain, and local plastic deformation is a prerequisite for the initiation and propagation of fatigue cracks. This method is particularly suitable for the estimation of fatigue life under random loads. The local strain method was used to estimate the initial life of material fatigue cracks during CE, and it was assumed that the root cracks of this model (Fig. 1b) were caused by uniaxial fatigue element cracking. In this model, the strain fatigue life could be considered the initial life of a cavitation crack at a certain position. When N_i bubbles collapsed and impacted a specific position of the specimen, fatigue cracks began to initiate at that position.

Manson [26] and Coffin [27] proposed the fatigue crack initial life predictive equations in the elastic range and plastic range, respectively (Eqs. (3) and (4)). Equation (5) is Manson-Coffin equation by considering Eqs. (3) and (4).

$$\frac{\Delta\varepsilon_e}{2} = \frac{\sigma'_f}{E} \cdot \left(2N_f\right)^b, \tag{3}$$

$$\frac{\Delta\varepsilon_p}{2} = \varepsilon_f \cdot \left(2N_f\right)^C, \tag{4}$$

$$\frac{\Delta\varepsilon_T}{2} = \frac{\Delta\varepsilon_e}{2} + \frac{\Delta\varepsilon_p}{2} = \frac{\sigma'_f}{E} \cdot \left(2N_f\right)^b + \varepsilon_f \cdot \left(2N_f\right)^C. \tag{5}$$

According to Hook's law, when the load on the specimen is in the elastic deformation stage, the elastic strain $\Delta\varepsilon_e$ satisfies Eq. (6).

$$\Delta\varepsilon_e = \frac{\Delta\sigma}{E}. \tag{6}$$

In an elastic-plastic state, the relationship between the stress and strain of the material satisfies the Hollomon equation (Eq. (7)). When the smooth specimen undergoes the same stress-strain process as the plastic deformation zone at the root of the notched specimen, the fatigue life of the smooth specimen can be equivalent to the crack formation life of the notched specimen, and the maximum strain ε at the root of the notched specimen and maximum stress S satisfy Neuber's rule (Eq. (8)) [28].

$$S = K \cdot \varepsilon_p^n, \tag{7}$$

$$S \cdot \varepsilon = \frac{1}{E}(K_t \cdot \sigma)^2. \tag{8}$$

Considering Eqs. (3) and (6), Eqs. (4), (7), and (8), respectively, the relationship between the constant-amplitude load and the initial fatigue crack life under that load satisfies Eq. (9).

$$N_f = \begin{cases} \frac{1}{2} \cdot \left(\frac{\Delta\sigma}{2\sigma'_f}\right)^{\frac{1}{b}}, & \Delta\sigma \le \sigma_{0.2}; \\ \left(\frac{1}{2}\right)^{\frac{1+C}{C}} \cdot \left(\frac{1}{ES_f\varepsilon_f}\right)^{\frac{1}{(n+1)C}} (K_t\Delta\sigma)^{\frac{2}{(n+1)C}}, & \Delta\sigma > \sigma_{0.2}. \end{cases} \tag{9}$$

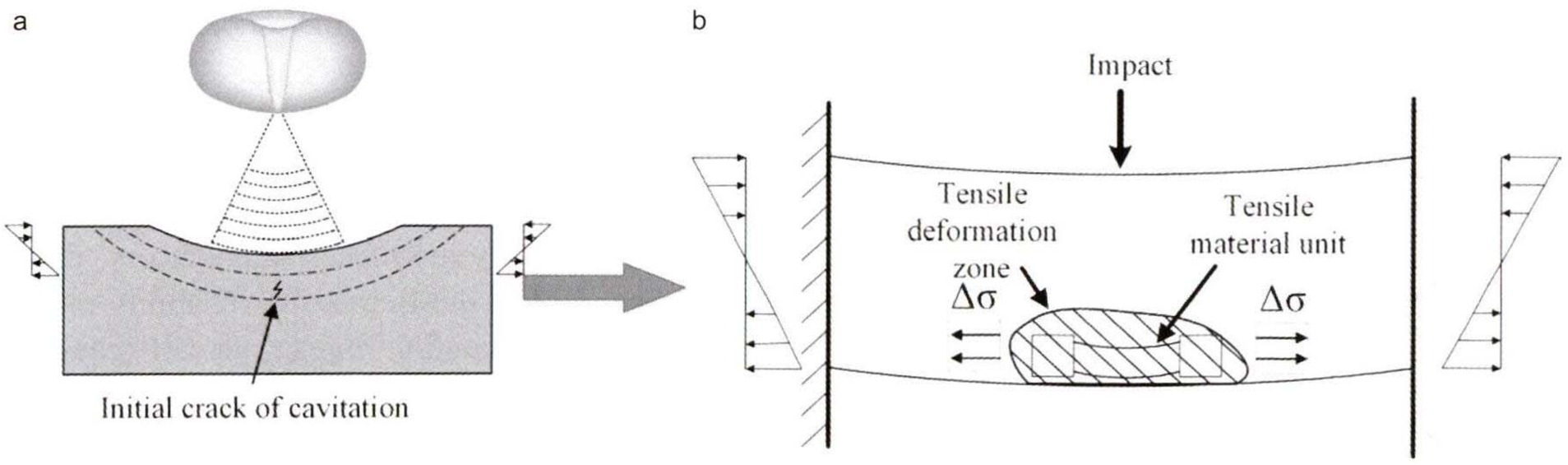

Figure 1 **a** Model of cavitation crack initiation. **b** Uniaxial fatigue element in the plastic zone at the root of the test specimen with low energy multiple times.

We can take $\alpha = \left(\frac{1}{ES_f\varepsilon_f}\right)^{\frac{\beta}{2}}$ and $\beta = \frac{2}{(1+n)C}$, Eq. (9) can be simplified to Eq. (10).

$$N_f = \begin{cases} \frac{1}{2}\cdot\left(\frac{\Delta\sigma}{2\sigma_f}\right)^{\frac{1}{b}}, & \Delta\sigma \le \sigma_{0.2}; \\ \left(\frac{1}{2}\right)^{\frac{1+C}{C}}\alpha\cdot(K_t\Delta\sigma)^{\beta}, & \Delta\sigma > \sigma_{0.2}. \end{cases} \tag{10}$$

Equation (10) only considers the fatigue crack initiation when the material is subjected to multiple impacts with small energy under constant load. In the process of CE, the distance between the collapse position of bubbles and surface of sample is different; thus, the impact on the sample is also different. Under the action of a large energy impact, the nominal stress of the material is also significant, and the fatigue crack initiation life is short. Under a smaller energy impact, the fatigue crack initiation life becomes longer. Aiming at fatigue crack initiation life under variable amplitude load, Miner [29] first proposed the linear damage accumulation theory. The linear damage accumulation theory believes that the damage (D) of a material under a single load and the number of cycles of component failure under that load (the fatigue life of the material under a certain load, N_f) satisfy Eq. (11).

$$D = \frac{1}{N_f}. \tag{11}$$

The total damage of the material (D_t) can be expressed by Eq. (12).

$$D_t = \sum_{i=1}^{k}\frac{n_i}{N_{f_i}}. \tag{12}$$

It is considered that the material is damaged when the total damage of the material is equal to 1.

Assuming that the probability of a bubble with nominal stress of $\Delta\sigma_j$ on the surface of the material is P_j , and assuming that N_i bubbles collapse and impact a particular fixed position on the surface, where cavitation cracks are generated due to fatigue, then N_i meets Eq. (13). Therefore, according to mechanical properties, considering Eqs. (10) and (13), the number of bubble impacts experienced by the initial cavitation cracks at a certain position of the material can be obtained.

$$D_t = \sum_{j=1}^{k}\frac{N_i\cdot P_j}{N_{f_j}} = 1. \tag{13}$$

Since the location of the cavitation bubbles impacting the surface is random, according to the geometrical probabilities, the probability p of the bubbles acting on a certain position on the specimen can be expressed by Eq. (14).

$$p = \frac{S}{S_0}. \tag{14}$$

Assuming that the position of each bubble is random and independent, if the total number of bubbles acting on the entire cavitation zone is M, the probability of at least m bubbles acting on a certain place can be represented by Eq. (15).

$$P(m) = 1 - \sum_{i=1}^{m}\binom{M}{i}p^i(1-p)^{M-i}. \tag{15}$$

When the probability ($P(m = N_i)$) of at least N_i bubbles acting on a certain point of the sample is higher than 99%, it is considered that the point has fatigue cracks. M is equal to M_f if M satisfies the inequality Eq. (16).

$$P(m = N_i) = 1 - \sum_{i=1}^{m}\binom{M}{i}p^i(1-p)^{M-i} \ge 99\%. \tag{16}$$

The crack nucleation process is completed when the number of bubbles that impact the sample surface is greater than M_f. The cracks begin to expand and connect, and the material begins to fall off, resulting in apparent cavitation weight loss. This marks the end of the cavitation incubation period, and CE enters the accelerated destruction.

In the process of ultrasonic CE, the number of bubbles generated per unit time can be considered constant, so the length of CE incubation period (t_i) and minimum total number of impacts (M_f) should meet Eq. (17).

$$t_i(h) = \frac{M_f}{f_c\times 60\times 60}, \tag{17}$$

where f_c is the frequency of cavitation impact on the surface.

3. Materials and experiments

3.1 Materials

In this paper, DSS surfacing layer was obtained by TIG powder surfacing, and tensile test and CE test were performed to verify the accuracy of the model. The nominal composition of the designed surfacing layer is shown in Table 1.

In order to prevent the alloying elements from being diluted by the carbon steel substrate (Q235), a transition layer must be prepared on the substrate. The transition layer was prepared by melt inert-gas welding (MIG) method. The welding wire was ER2209 with ϕ1.2, and the shielding gas was argon (Ar) with a purity of 99.99%. The DSS surfacing layer was obtained on the transition layer by TIG synchronous powder feeding surfacing method. The surfacing layer was remelted after the powder surfacing. The gas used in welding shielding and powder feeding were both Ar. The schematic diagram of TIG surfacing equipment is shown in

Table 1 Nominal composition of the surfacing layer (wt.%)

Cr	Ni	Mo	Nb	C	N	Fe
22	9	3	0.75	< 0.03	0.15	Balance

Fig. 2. Before surfacing, a VH-2 powder mixer was used to mix the alloy powder used, and the mixing time was longer than 2 h. The welding process parameter is shown in Table 2.

3.2 Experiments

After the surfacing welding, the TCXC1700 resistance furnace was used to perform solution treatment on the surfacing layer to homogenize the structure. The heat treatment parameters and sample numbers are shown in Table 3.

The location and the size of the tensile specimen are shown in Fig. 3. The tensile test was carried out on the UTM5105 (accuracy level: 0.5) universal testing machine.

The samples used for CE were cut from the center of the surfacing layer. The eroded surfaces of the CE samples are close to the top of the surfacing layer and belong to the last layer of surfacing metal. The samples were rubbed to 1200 mesh with sandpaper and then polished in sequence with W2.5 and W1 diamond abrasive paste. A Qsonica Q700 magnetostrictor was used to carry out the cavitation test at room temperature. The test power was 700 W, the vibration frequency was 20 kHz, and the horn amplitude was 60 μm. Distilled water was used as the cavitation medium. A balance with an accuracy of 0.1 mg was used to measure the weight change of the sample during CE. The cavitation equipment and sample size are shown in Fig. 4.

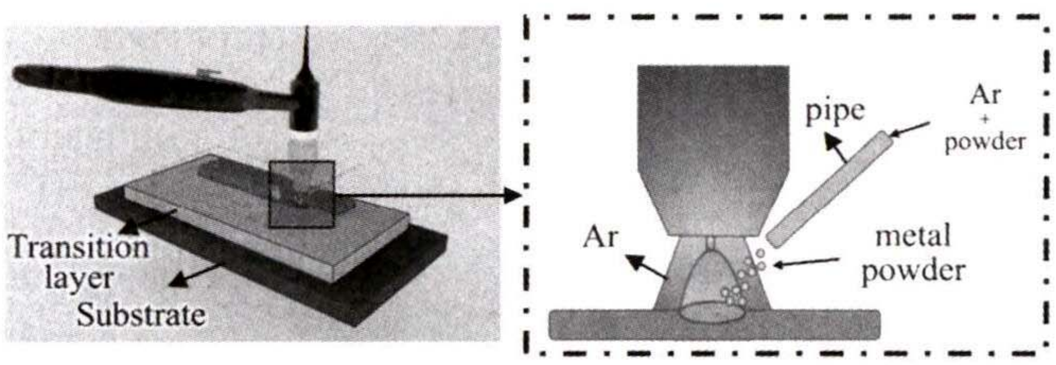

Figure 2 Welding equipment diagram.

3.3 Results

The structure of the welded surfacing layer is very complicated, as shown in Fig. 5. Due to the multiple thermal cycles in the surfacing process and the use of the remelting process, the heat input of the surfacing layer is relatively large. Large heat input resulted in the appearance of dendritic crystals and widmanstatten structures in the middle of the surfacing layer, while the top of the surfacing layer was almost entirely austenite. However, the microstructure becomes simple after heat treatment. The microstructure is mainly composed of austenite and equiaxed ferrite. In addition, the content of ferrite increased slightly.

Figure 6 is the tensile test results of the surfacing layer of DSS. It can be seen from Fig. 6 that the yield strength of TG was 446 MPa, and the tensile strength can reach 804 MPa. The yield strength of the solution-treated TGS-1 and TGS-2 were both 355 MPa, but the tensile strength of TGS-1 was 741 MPa, slightly higher than that of TGS-2 (728 MPa). From Fig. 6b, it can also be seen intuitively that the plastic elongation at the maximum force of the TG surfacing layer was 41.6%. The maximum force non-proportional elongation, elongation after fracture, and reduction of area of TGS-1 were also higher than those of TGS-2.

Table 2 Parameters of the surfacing welding process

Welding parameters	Welding method	Welding current I (A)	Welding voltage U (V)	Welding speed v (mm min^{-1})	Shield air flow q (L s^{-1})
Transition layer	MIG	200	25	150	15
Test group	TIG	200	–	150	20
Remelting	TIG	210	–	150	20

Table 3 Parameters of the heat treatment

Heating Rate (°C/min)	Holding temperature T (°C)	Holding time t (min)	Type of cooling	Sample number
–	–	–	–	TG
10	1150	90	Water quench	TGS-1
10	1250	90	Water quench	TGS-2

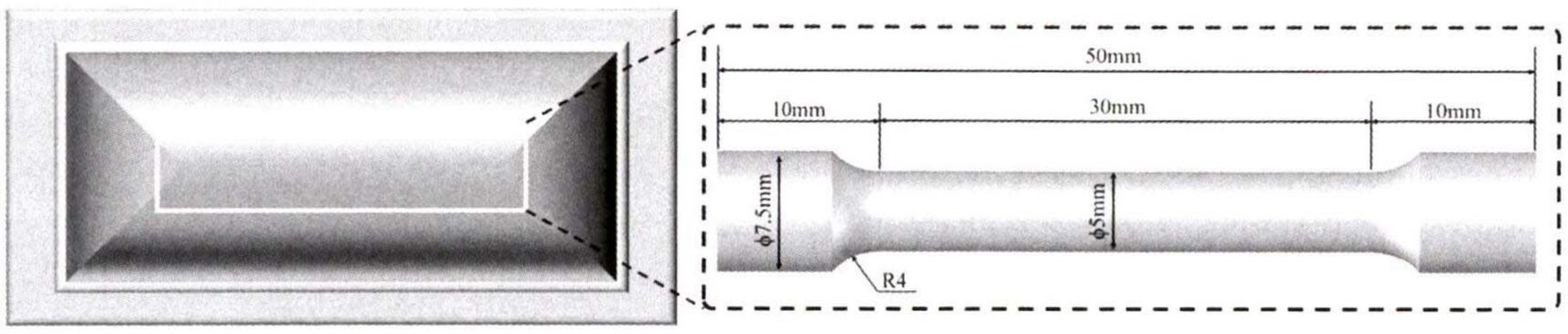

Figure 3 The location and the size of tensile test sample.

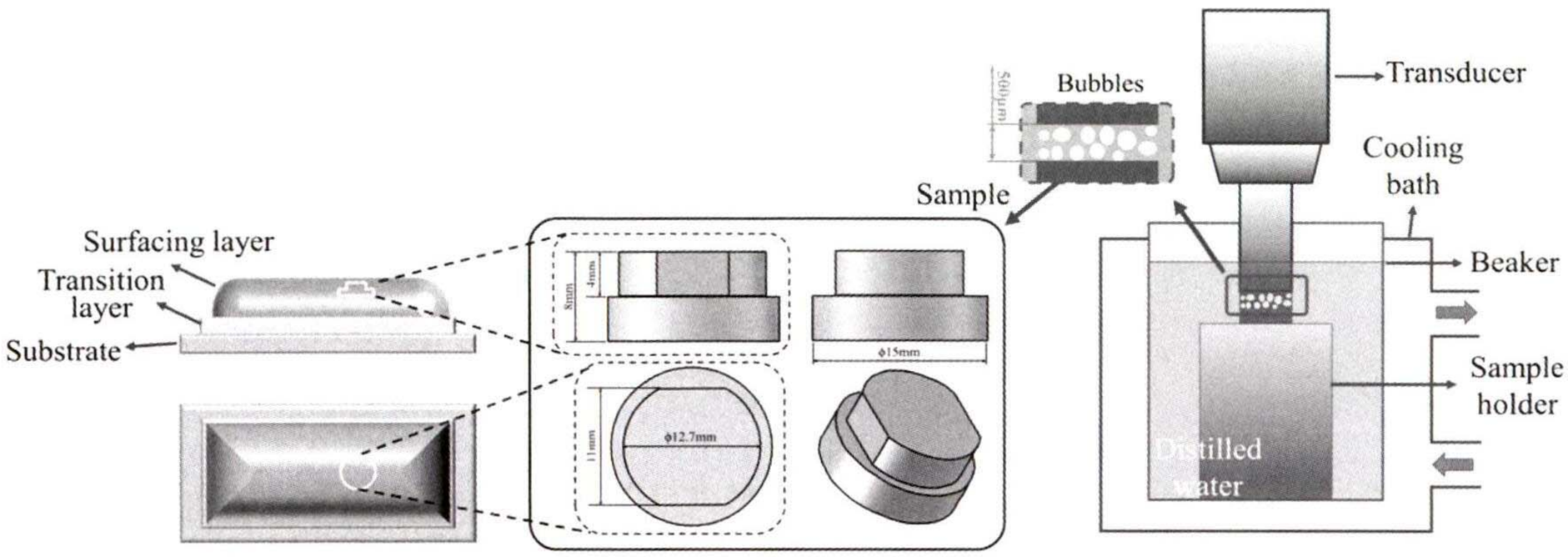

Figure 4 Ultrasonic CE equipment and the size of test samples.

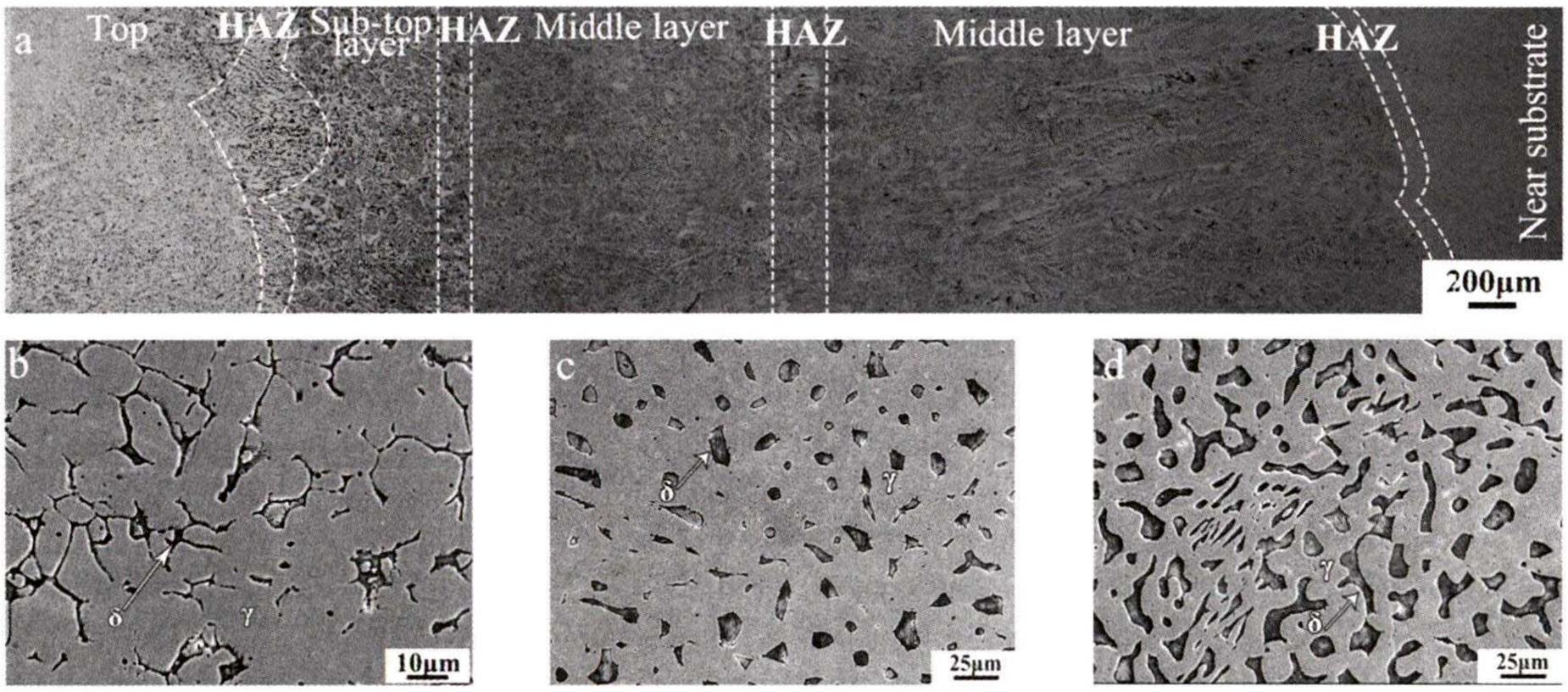

Figure 5 The microstructure of samples. **a** The cross-sectional microstructure of TG, **b-d** the microstructure of the top of the surfacing layer of TG, TGS-1, and TGS-2.

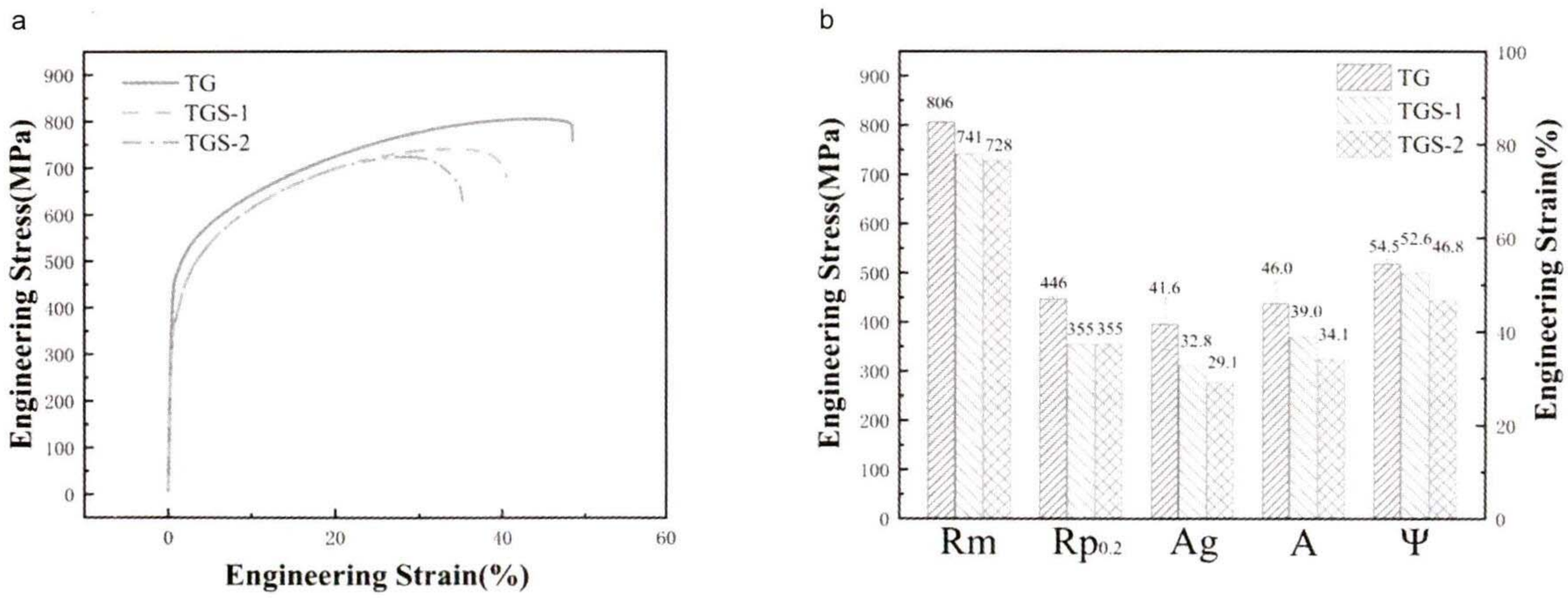

Figure 6 Mechanical properties of the surface layer. **a** Tensile curves, **b** characteristic data.

The cumulative weight loss of CE was plotted as a function of time. The results are shown in Fig. 7. The cumulative weight loss of the DSS surfacing layer shows a non-linear relationship with the increase of time. Within 3 h, the cumulative weight loss of the surfacing layer is minimal, all less than 0.5 mg. Then, the cavitation weight loss began to show a more obvious increase with time. As shown by the cavitation weight loss rate-time curve, the curve can be di-

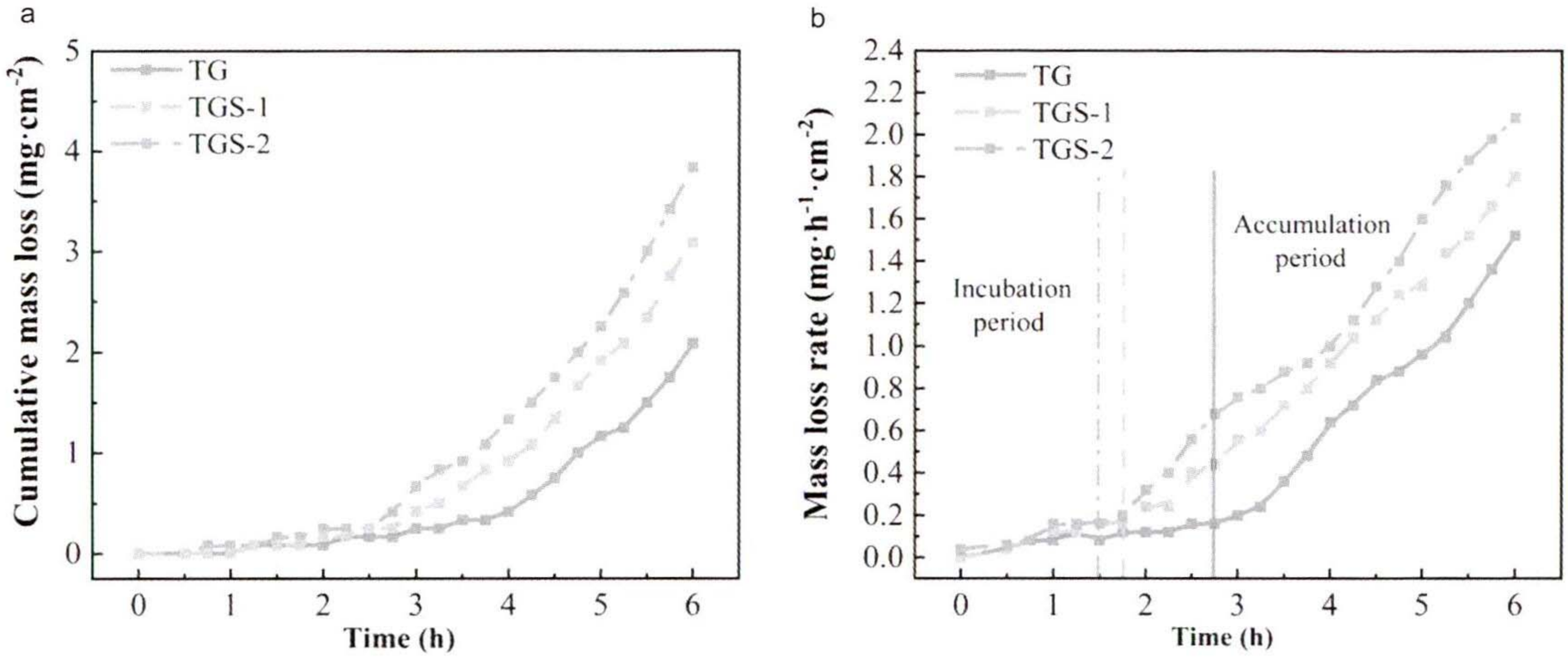

Figure 7 **a** Cumulative mass loss as a function of time for surface layer. **b** Mass loss rate as a function of time for surface layer.

vided into incubation and accumulation periods. During the incubation period of CE, the weight loss rate was low and almost did not change with time. During the accelerated destruction period, the rate of CE increased with time. The incubation period of TG, TGS-1, and TGS-2 is about 2.75 h, 1.75 h, and 1.5 h, respectively.

4. Parameters and calculation results

In order to solve the predictive equation, it is necessary to calculate and explain the relevant parameters used in the equation.

4.1 Parameter confirmation

4.1.1 Strength coefficient K and deformation hardening index n

Equations (18) and (19) were used to process the tensile curve and calculate the true stress and true strain of the material. Then, take the logarithms on both sides of Eq. (7), and substitute the value of true stress and true strain at the yield point and tensile strength point of the material.

$$S = \sigma(1+\varepsilon), \tag{18}$$

$$\varepsilon_T = \ln(1+\varepsilon), \tag{19}$$

$$\ln S_{p0.2} = \ln K + n\ln\varepsilon_{0.2}, \tag{20}$$

$$\ln S_m = \ln K + n\ln\varepsilon_m. \tag{21}$$

It can be solved by considering Eqs. (20) and (21).

$$n = \ln\left(\frac{S_f}{S_{0.2}}\right) \Big/ \ln\left(\frac{\varepsilon_f}{\varepsilon_{0.2}}\right) = \ln\left(\frac{S_f}{S_{0.2}}\right) \Big/ \ln\left(500\varepsilon_f\right), \tag{22}$$

$$K = \left[(\varepsilon_{0.2}\cdot\varepsilon_f)^{-n}\left(S_{0.2}\cdot S_f\right)\right]^{1/2} = \left[\left(0.002\cdot\varepsilon_f\right)^{-n}\left(S_{0.2}\cdot S_f\right)\right]^{1/2}. \tag{23}$$

4.1.2 Fatigue strength coefficient σ'_f and fatigue ductility index C

Richman and McNaughton [21] counted the relationship between σ'_f and fracture strength (σ_f) of different materials and found that the two are almost equal. From the tensile test data, we can get the tensile force (F_f) and the cross-sectional area (A_f) of the sample after fracture, then σ_f can be obtained by Eq. (24).

$$\sigma'_f = \sigma_f = \frac{F_f}{A_f}. \tag{24}$$

The book [30] indicates that the C value of the material can be estimated with an empirical Eq. (25).

$$C = -\lg\left[3.31\varepsilon_f^{0.25} / \sqrt[3]{1-81.8\left(\sigma_f/E\right)(1+\Psi)^{0.179}}\right]. \tag{25}$$

Based on the above equation, through repeated analysis and calculation, it is more appropriate to use Eq. (26) to estimate the C value in this paper.

$$C = 0.78\lg\left[3.31\varepsilon_f^{0.25} / \sqrt[3]{1-81.8\left(\sigma_f/E\right)(1+\Psi)^{0.179}}\right] - 0.033. \tag{26}$$

4.1.3 Probability of cavitation with different impact energy

Plesset and Ellis [31] believe that the pulse pressure produced by the collapse of cavitation bubbles is about 350 MPa to 900 MPa. Assuming that the pulse pressure value generated by collapse of bubbles in the fluid is random and with equal probability, then the probability density function of the stress value distribution can be expressed as Eq. (27), and the probability of the occurrence of a bubble (P_i) with nominal stress ($\Delta\sigma_i$) on the surface can be expressed as Eq. (28). The initial life N_i of a cavitation crack at a certain position satisfies Eq. (13).

$$f(\Delta\sigma_i) = \begin{cases} \dfrac{1}{550}, & 350 < \Delta\sigma_i < 900; \\ 0, & \text{other.} \end{cases} \tag{27}$$

$$P_i = \frac{\mathrm{d}(\Delta\sigma_i)}{550}. \tag{28}$$

4.1.4 Single bubble action range

Lim et al. [32] measured the size of cavitation pits formed by ultrasonic cavitation and used the Weibull model to calculate the probability distribution of the size of cavitation pit. The results are shown in Fig. 8. The average diameter of the pits left by the collapse of a single bubble on the surface of the sample is 31.2 μm, and the working area of the cavitation pit acting on a certain place can be obtained by Eq. (14). The calculation result is 0.000006.

4.1.5 The frequency of cavitation impact on the surface of the sample

In ultrasonic CE tests, cavitation bubbles are generated by the ultrasonic probe in the lower approximate cylindrical region, which then collapses and impacts the surface of the sample, as shown in Fig. 9. At this time, the ratio of the volume of gas to liquid (gas hold-up, η) of the area under ultrasonic probe can be expressed by Eq. (29). Therefore, if we know the range of cavitation damage (A_d), the volume of the bubbles (V_c), and the cavitation rate (η), the frequency of the cavitation impact on the surface of the sample can be obtained according to Eq. (30).

$$\eta = \frac{V_c \times N_c}{V_l} = \frac{V_c \times N_c}{h \times A_d}. \tag{29}$$

Zhang et al. [33] calculated the influence of different ultrasonic frequencies on the void content in the liquid. Their research results showed that the gas hold-up near the ultrasonic probe is about 0.008 when the ultrasonic frequency is 20 kHz. Before the bubble collapses, the radius of the bubble ranges from 50 to 150 μm, and the average value is 100 μm. The eroded area by CE is about 119.38 mm^2.

Assuming that all the bubbles generated by the vibration act on the surface of the sample, N_c is the number of cavities generated by each vibration, and 20000 is the vibration frequency, the frequency of the cavitation impacting the sample can be obtained by Eq. (30).

$$f_c = 20000 \times N_c. \tag{30}$$

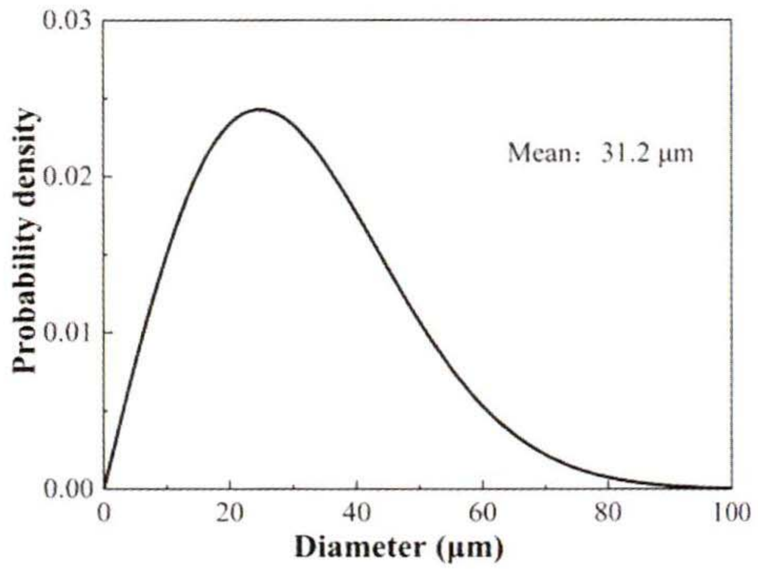

Figure 8 Probability density of the size of cavitation craters [32].

4.2 Calculation result

The parameters used and the strain fatigue life N_i of cavitation cracks at a certain position of the material are shown in Table 4. According to the N_i value of the surfacing layer under different conditions, the *M-P* ($m = N_i$) curves were plotted (Fig. 10). M_f is the value of M when $P(m = N_i) \approx 99\%$ in the curve.

Combined with the value of f_c, it can be determined that the predictive equation of the material cavitation incubation period under the conditions in this paper is Eq. (31).

$$t_i(h) = \frac{M_f}{5832000000}. \tag{31}$$

Table 5 lists the actual values, calculated values, and errors

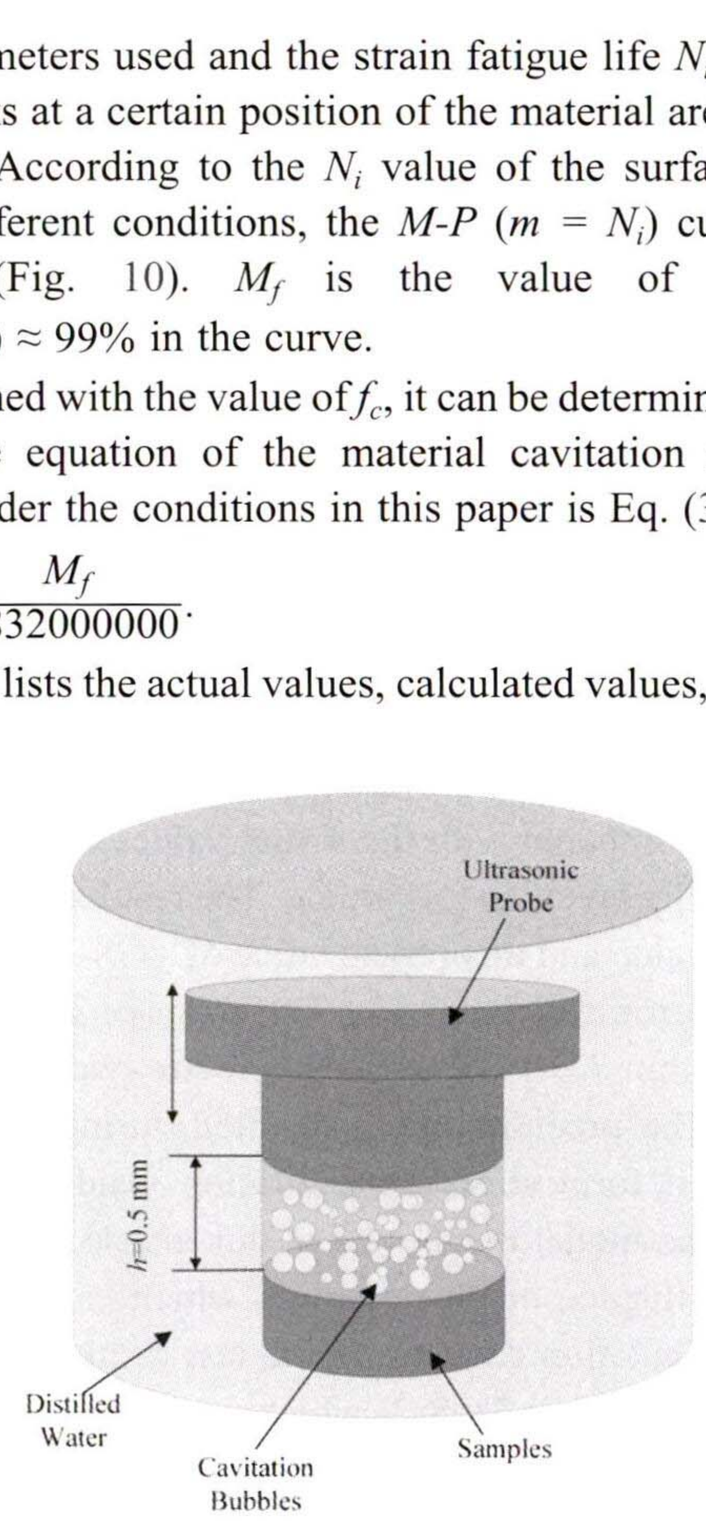

Figure 9 Schematic diagram of cavitation test.

Table 5 The calculated value, actual value, and error of cavitation incubation period

Samples	Calculated value (h)	Actual value (h)	Error (%)
TG	2.82	2.75	2.5
TGS-1	1.81	1.75	3.3
TGS-2	1.62	1.5	8.1

Table 4 Parameters used in this model

Samples	$S_{0.2}$ (MPa)	S_m (MPa)	ε_m (%)	Ψ (%)	σ_f (MPa)	n	K	C	β	α ($\times 10^{16}$)	N_i ($\times 10^4$)	N_c	f_c
TG	446	1141	35	54.5	1736	0.18	1383	−0.43	−3.95	3.99	9.25		
TGS-1	355	984	28	52.6	1455	0.21	1275	−0.40	−4.18	1.67	5.92	81	1620000
TGS-2	355	940	26	46.8	1203	0.2	1236	−0.38	−4.35	5.15	5.31		

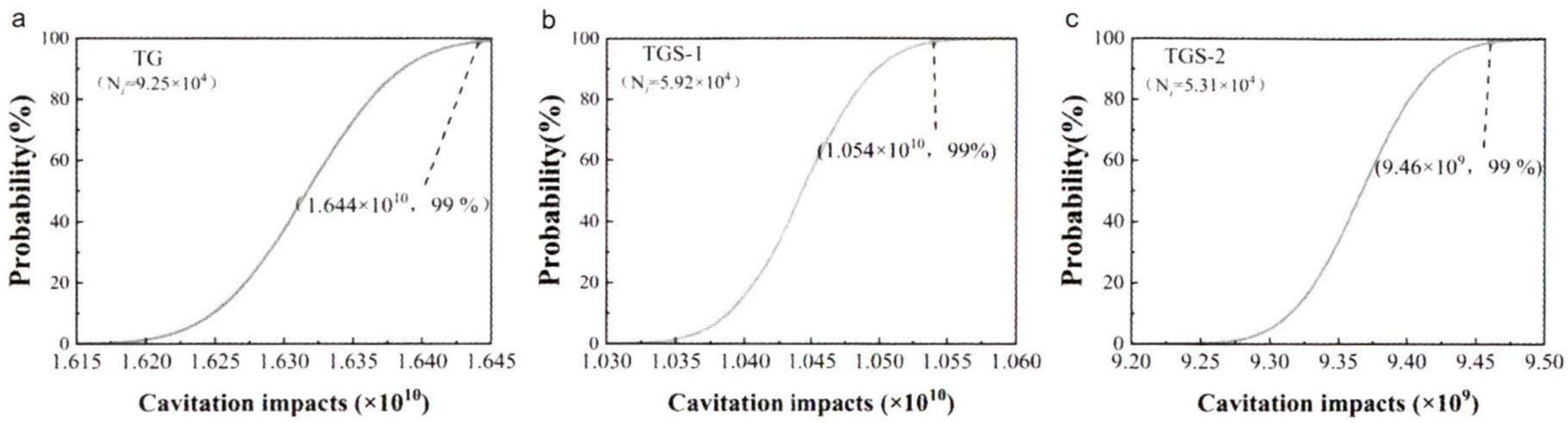

Figure 10 *M-P'* ($m = N_i$) curves. **a** TG, **b** TGS-1, **c** TGS-2.

for the incubation period of three groups surfacing layers. It can be seen from Table 5 that the errors between the actual values and calculated results of TG and TGS-1 are all within 3.5%. The error of TGS-2 surfacing layer is only 8.1%.

5. Conclusion

According to the loading process during CE, local strain fatigue theory, linear accumulation theory of fatigue damage, and Bernoulli probability model were used to derive the predictive equation for the cavitation period in benign media. The cavitation incubation period of the material was estimated and compared with the actual values of three groups DSS surfacing layers in this article. The results show that the calculated value and theoretical value of TGS-2 sample have the largest error, which is 8.1%. The errors of TG and TGS-1 are both within 3.5%. However, there are two points to explain. (1) The precipitations generated during sample preparation will form stress concentration inside the sample. However, the model mentioned in this article does not consider the influence of precipitation, which causes the error between calculation results and the test results. This deviation was apparent in TGS-2, which with more precipitates. (2) During the cavitation test, the mass loss rate was calculated based on the weight measurement of the sample every 0.25 h. Therefore, the measured cavitation incubation period is a multiple of 0.25 h, which leads to an error between the measured value and the actual incubation period.

This work was supported by the National Natural Science Foundation of China (Grant No. 51879089). Material preparation, data collection, and analysis were performed by Yefeng Bao, Bingqi Xie, Qining Song, and Yongfeng Jiang. The first draft of the manuscript was written by Chong Cao. Nan Xu provided language help and writing assistance.

1 L. A. Espitia, and A. Toro, Cavitation resistance, microstructure and surface topography of materials used for hydraulic components, Tribol. Int. **43**, 2037 (2010).
2 W. Wang, T. Tang, Q. D. Zhang, X. F. Wang, Z. Y. An, T. H. Tong, and Z. J. Li, Effect of water injection on the cavitation control:experiments on a NACA66 (MOD) hydrofoil, Acta Mech. Sin. **36**, 999 (2020).
3 Q. Chen, Y. Liu, Q. Wu, Y. Wang, T. Liu, and G. Wang, Global cavitation patterns and corresponding hydrodynamics of the hydrofoil with leading edge roughness, Acta Mech. Sin. **36**, 1202 (2020).
4 K. Su, J. Wu, and D. Xia, Dual role of microparticles in synergistic cavitation-particle erosion: Modeling and experiments, Wear **470-471**, 203633 (2021).
5 S. Cleve, M. Guédra, C. Mauger, C. Inserra, and P. Blanc-Benon, Microstreaming induced by acoustically trapped, non-spherically oscillating microbubbles, J. Fluid Mech. **875**, 597 (2019).
6 M. Mohammadzadeh, F. Li, and C. D. Ohl, Shearing flow from transient bubble oscillations in narrow gaps, Phys. Rev. Fluids **2**, 014301 (2017).
7 T. B. Benjamin, and A. T. Ellis, A discussion on deformation of solids by the impact of liquids, and its relation to rain damage in aircraft and missiles, to blade erosion in steam turbines, and to cavitation erosion —The collapse of cavitation bubbles and the pressures thereby produced against solid boundaries, Phil. Trans. R. Soc. Lond. A **260**, 221 (1966).
8 Z. Li, J. Han, J. Lu, and J. Chen, Cavitation erosion behavior of Hastelloy C-276 nickel-based alloy, J. Alloys Compd. **619**, 754 (2015).
9 A. M. Abdel Fattah, and M. A. Sidkey, Cavitational damage of titanium in molten lead, Bull. Mater. Sci. **5**, 179 (1983).
10 C. G. Stephanis, J. G. Hatiris, and D. E. Mourmouras, The process (mechanism) of erosion of soluble brittle materials caused by cavitation, Ultrason. Sonochem. **4**, 269 (1997).
11 W. J. Tomlinson, and M. G. Talks, Erosion and corrosion of cast iron under cavitation conditions, Tribol. Int. **24**, 67 (1991).
12 K. Y. Chiu, F. T. Cheng, and H. C. Man, Evolution of surface roughness of some metallic materials in cavitation erosion, Ultrasonics **43**, 713 (2005).
13 X. Long, H. Yao, and J. Zhao, Investigation on mechanism of critical cavitating flow in liquid jet pumps under operating limits, Int. J. Heat Mass Transfer **52**, 2415 (2009).
14 P. V. Marques, and R. da Exaltação Trevisan, An SEM-based method for the evaluation of the cavitation erosion behavior of materials, Mater. Charact. **41**, 193 (1998).
15 C. Meena, and V. Uthaisangsuk, Micromechanics based modeling of effect of sigma phase on mechanical and failure behavior of duplex stainless steel, Metall. Mater. Trans. A **52**, 1293 (2021).
16 B. J. Yoon, and Y. S. Ahn, Effect of Mo addition on aging behavior of

TRIP-aided duplex stainless steel, Mater. Charact. **173**, 110946 (2021).

17 T. Wan, N. Xiao, H. Shen, and X. Yong, The effect of chloride ions on the corroded surface layer of 00Cr22Ni5Mo3N duplex stainless steel under cavitation, Ultrason. Sonochem. **33**, 1 (2016).

18 K. Selvam, P. Mandal, H. S. Grewal, and H. S. Arora, Ultrasonic cavitation erosion-corrosion behavior of friction stir processed stainless steel, Ultrason. Sonochem. **44**, 331 (2018).

19 Q. Huang, and Z. Zhong, Cavitation-induced damage model of soft materials in exposure to high-intensity focused ultrasound, Acta Mech. Sin. **36**, 1058 (2020).

20 Z. Song, and S. Cai, Cavitation dynamics in a vitrimer, Acta Mech. Sin. **37**, 767 (2021).

21 R. H. Richman, and W. P. McNaughton, Correlation of cavitation erosion behavior with mechanical properties of metals, Wear **140**, 63 (1990).

22 A. Karimi, and W. R. Leo, Phenomenological model for cavitation erosion rate computation, Mater. Sci. Eng. **95**, 1 (1987).

23 Y. Long, X. Long, and B. Ji, LES investigation of cavitating flows around a sphere with special emphasis on the cavitation-vortex interactions, Acta Mech. Sin. **36**, 1238 (2020).

24 S. Hattori, and R. Ishikura, Revision of cavitation erosion database and analysis of stainless steel data, Wear **268**, 109 (2010).

25 F. Zhu, H. Yang, B. Wang, Y. Dai. and P. He, Fatigue crack initiation life of aviation duct bending test, Chin. Q. Mech. **41**, 519 (2020).

26 S. S. Manson, Behavior of materials under conditions of thermal stress, Nasa Tnd (1954).

27 L. Coffin, A study of the effects of cyclic thermal stresses on a ductile metal, Ryūmachi **76**, 931(1954).

28 Y. Zou, and G. Hu, Estimation of the initiation life of multi-impact fatigue cracks in 0.4C-Cr-Ni-Mo-Si steel, Acta Aeronaut. Sinica **9**, 487 (1989).

29 M. A. Miner, Cumulative damage in fatigue, J. Appl. Mech. **12**, 159 (1945).

30 Manual of Strain Fatigue Analysis, Science and Technology Committee of the Ministry of Aviation Industry (1987).

31 M. S. Plesset, and A. T. Ellis, On the mechanism of cavitation damage, Trans. ASME **77**, 1055 (1955).

32 Y. Lim, P. Murugesan, S. Jung, and H. Lee, Evaluation of residual stress from ultrasonic cavitation peening using cavitation pit analysis and FEA, Int. J. Mech. Sci. **198**, 106352 (2021).

33 A. Zhang, Z. Yang, R. Xia, Q. Ding, and Y. Zhang, Research on the influence of ultrasonic frequency and tubular type on ultrasonic cavitation effect, Chem. Mach. **43**, 517 (2016).

非腐蚀介质中双相不锈钢堆焊层的空蚀孕育期预测模型研究

包晔峰, 曹冲, 谢秉錡, 宋亓宁, 蒋永锋, 许楠

摘要 为了估算在超声波空蚀条件下不锈钢的空蚀孕育期, 本文分析了空蚀过程中试样的受载过程, 使用局部应变理论和累计损伤理论, 并结合伯努利概率模型, 推导了使材料萌生疲劳裂纹所需的最小空泡冲击数, 并给出了材料空蚀孕育期的估算公式; 通过TIG粉末堆焊的方法制作了双相不锈钢试样, 对其进行拉伸和超声波空蚀, 将拉伸数据用于空蚀孕育期计算; 结果表明因实际测量精度, 以及试样中可能存在的析出相和微裂纹的影响, 会使计算结果出现一定程度的误差, 最大误差为8.1%, 其余两组误差均在3.5%以内.